

# Prediction Method for Unsteady Axisymmetric Flow over Parachutes

J. H. Strickland\*

Sandia National Laboratories, Albuquerque, New Mexico 87185

A method which is capable of solving the axisymmetric flowfield over bluff bodies consisting of thin shells such as disks, partial spheres, rings, and other such shapes is presented in this article. The body may be made up of several shells whose edges are separated by gaps. The body may be moved axially according to arbitrary velocity time histories. In addition, the surfaces may possess axial and radial degrees of flexibility such that points on the surfaces may be allowed to move relative to each other according to some specified function of time. The surfaces may be either porous or impervious. The present solution technique is based on the axisymmetric vorticity transport equation. This technique requires relatively large numbers of ring vortices (1000 or more) to obtain good simulations. Since the direct calculation of perturbations from large numbers of ring vortices is computationally intensive, a fast multipole method was used to greatly reduce computer processing time. Several example calculations are presented for disks, disks with holes, hemispheres, and vented hemispheres. These results are compared with steady and unsteady experimental data.

## Introduction

MOTIVATION for the present work comes from a need to understand the unsteady flow around high-performance parachute systems, especially during the inflation process. Attempts to use Navier-Stokes flow solvers for this problem have not progressed very far to date, largely because of the problems associated with the moving boundaries which require that a new grid be generated at each time step. The most successful numerical treatments of bluff body flows to date have involved the use of vortex methods. The general analytical approach for solving bluff body flow problems with vortex methods is to simulate regions of vorticity in the wake flow with discrete vortices which are generated at points on the bluff body. Clements<sup>1</sup> gives a comprehensive review of wake modeling in two-dimensional flows using discrete vortices. Solid boundaries are generated by the use of conformal mapping, panel methods, or by other potential flow methods. Excellent reviews of vortex methods are given by Sarpkaya,<sup>2</sup> Saffman and Baker,<sup>3</sup> and Leonard.<sup>4</sup> There have been several papers written concerning vortex methods as applied to flow around "parachute-like objects" many of which are two-dimensional planar flows. A paper by Sarpkaya<sup>5</sup> provides a review of some of the more recent works. The present work provides an application of the vortex method to axisymmetric flows utilizing a fast solver for large numbers of ring vortices. The resulting method allows one to obtain solutions to practical problems of interest in the field of parachute aerodynamics.

## Method of Analysis

A very brief summary of the method of analysis will be given in this article. Readers who are interested in more details are referred to Ref. 6.

### General

The general methodology provides a means by which a solution to the vorticity equation may be obtained. The vor-

ticity equation is obtained by taking the curl of the Navier-Stokes equations for a fluid of constant density and viscosity.<sup>7</sup> For planar and axisymmetric flows, the vorticity equation reduces to

$$\frac{\partial \omega}{\partial t} + (\vec{u} \cdot \nabla) \omega = \nu \nabla^2 \omega \quad (1)$$

where  $\omega$  is the scalar vorticity and  $\nu$  is the kinematic viscosity of the fluid. From Eq. (1) it can be seen that a description of the flow may be obtained by modeling the transport and diffusion of the vorticity in the flow. Since many flows exhibit compact regions of vorticity, only a fraction of the flowfield must be modeled to obtain results. The vorticity is generated only at the body surfaces for constant density flows. Away from the wall the viscous diffusion term tends to be small compared to the transport terms. Neglecting viscous effects reduces Eq. (1) (written in terms of the circulation  $\Gamma$ ) to the well known Kelvin's theorem:

$$\frac{\partial \Gamma}{\partial t} + (\vec{u} \cdot \nabla) \Gamma = 0 \quad (2)$$

The problem, therefore, reduces to the transport of fluid particles (vortices) containing a fixed amount of circulation  $\Gamma$ . While the circulation of the fluid particles is produced by viscous processes at the wall, the exact flow behavior at the wall does not have to be modeled in order to determine the value of  $\Gamma$  for each vortex which is generated. The major consequence which arises from not modeling the details of the diffusion process at the wall is that the core geometry of each vortex cannot be accurately obtained. For high Reynolds number bluff-body flows this is not a significant problem, in that the results are not very sensitive to choices for initial core size and initial placement of vortices relative to the wall.

In order to develop a general understanding of the approach which will be used in the present work, reference is made to the crude depiction of the vorticity field near a parachute as shown in Fig. 1. Initially, there are no vortices in the flow. In order to satisfy the boundary conditions at the surface of the parachute, a number of ring vortices are placed along the parachute surfaces. The circulation strengths of the vortices are calculated so as to satisfy the wall boundary conditions. Next, the flow solution is advanced by one time step. During this time step, the body surfaces move in some prescribed

Received Feb. 16, 1993; revision received May 7, 1993; presented as Paper 93-1217 at the RAeS/AIAA 12th Aerodynamic Decelerator Systems Technology Conference, London, England, UK, May 10-13, 1993; accepted for publication June 2, 1993. This paper is declared a work of the U.S. Government and is not subject to copyright protection in the United States.

\*Senior Member Technical Staff, Associate Fellow AIAA.

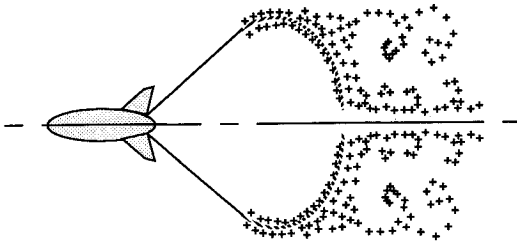


Fig. 1 Schematic of parachute vorticity.

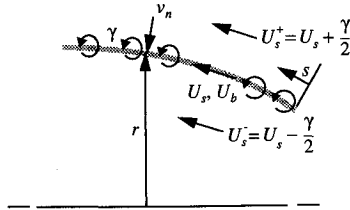


Fig. 2 Boundary conditions.

manner to a new position. They may move in a flexible manner if so desired (i.e., other than rigid body motion). The vortices are convected in the flow to new positions at the local fluid velocity. These velocities are calculated from formulas derived from considerations of the stream function produced by the system of vortices. Next, a new set of vortices is introduced at the surface. The circulation strengths are again calculated so as to satisfy the surface boundary conditions in conjunction with the previously shed set of vortices. This process is repeated for the desired number of time steps. Pressure distributions along the surface are calculated at each time step based on the strengths of the new surface vortices.

#### Surface Boundary Conditions

Boundary conditions for solid surfaces require that the normal and tangential velocity components relative to the surface be zero at the surface. The component of velocity normal to the surface  $v_n$  is given in terms of the stream function  $\psi$  by

$$v_n = -\frac{1}{r} \frac{d\psi}{ds} \quad (3)$$

It should be noted that  $v_n$  is relative to the inertial reference frame, not the body-fixed reference frame. Therefore, for an impervious surface, the required value of  $v_n$  is equal to the normal surface velocity.

The stream function for the flowfield is constructed by superimposing the stream functions of individual ring vortices which are given by Lamb<sup>8</sup>:

$$\psi = \frac{1}{2} \Gamma b r \int_0^\infty e^{-kx} J_1(kr) J_1(kb) dk \quad (4)$$

The ring radius is denoted by  $b$ , the axial distance from the ring by  $x$ , and the radial distance by  $r$ . The axial and radial velocities are given by

$$\begin{aligned} u &= \frac{1}{r} \frac{\partial \psi}{\partial r} \\ v &= -\frac{1}{r} \frac{\partial \psi}{\partial x} \end{aligned} \quad (5)$$

In order to satisfy the condition that the tangential velocity relative to the surface be equal to zero requires that a vortex sheet with strength equal to the edge velocity minus the tangential body velocity  $U_b$  be placed on the surface. Referring to Fig. 2, this means that a counterclockwise vortex sheet with strength  $U_s^+ - U_b$  would be placed on the top surface, and

a counterclockwise sheet with strength  $-U_s^- + U_b$  would be placed on the bottom surface.

In order to model surface porosity, one must first determine the scale of the porosity relative to the desired resolution of the flowfield. For instance, large slots in the surface might best be modeled using several shells, whereas a shell made up of a woven fabric would probably not be modeled as a series of individual threads. Thus, one can speak of geometric porosity and material porosity. The boundary conditions for surfaces possessing material porosity must be modeled in some approximate way since the detailed flow structure is not simulated.

For porous materials, the amount of flow through the surface is a function of the pressure drop across the surface. For instance, Koo and James<sup>9</sup> use a flow coefficient  $K$  which is related to the normal transpiration velocity  $v_{nt}$  through the surface and the pressure drop  $\Delta p$  across the surface by

$$K = \frac{\Delta p}{\frac{1}{2} \rho v_{nt}^2} \quad (6)$$

The coefficient  $K$  is obtained experimentally. The transpiration velocity  $v_{nt}$  is simply the normal velocity through the surface measured relative to the surface.

Modeling the tangential velocity at the "surface" is somewhat tentative since the exact behavior of the flow at the surface is dependent on the surface porosity geometry. One knows, however, that the tangential velocity at the surface should be equal to the tangential body velocity  $U_b$  for 0% porosity. On the other hand, as the porosity approaches 100%, the tangential velocity at the midplane of the surface should be equal to the tangential velocity induced by all of the vorticity in the flow at that point. An expression for the tangential wall velocity  $U_w$  which satisfies these constraints is given by

$$U_w = U_b(1 - \xi) + U_s \xi \quad (7)$$

Here,  $U_s$  is the tangential velocity induced by all of the vorticity in the flow at the surface midplane, and  $\xi$  is the porosity as the ratio of the open area to the total area. It can be seen that this equation yields the proper tangential wall velocity for 0% porosity ( $U_w = U_b$ ) and 100% porosity ( $U_w = U_s$ ). It should be noted that this model is not inconsistent with the fact that there is a jump in tangential velocity across screens set obliquely to a uniform flow.<sup>10</sup> As indicated in Fig. 2, the jump is equal to the strength of the surface vortex sheet  $\gamma$ .

In order to satisfy the tangential wall velocity condition, vorticity sheets must be placed on the positive and negative sides of the surface which have the following strengths:

$$\gamma^+ = U_s^+ - U_w \quad (8)$$

$$\gamma^- = -U_s^- + U_w$$

$$\Gamma^+ = (\Gamma/2) + (1 - \xi)(U_s - U_b)\Delta l \quad (9)$$

$$\Gamma^- = (\Gamma/2) - (1 - \xi)(U_s - U_b)\Delta l$$

These vortices are modeled using constant vorticity cores. The core radii  $a$  are arbitrarily chosen to be equal to one-half of the panel length  $\Delta l$ . Their centers are placed at a distance  $a$  away from the wall. It can be noted that the system of vortices crudely represents a layer of vorticity whose thickness is of the order  $\Delta l$ . If the effects of Reynolds number were being simulated, the thickness of this layer would be a function of the time step and the rate at which vorticity is diffusing away from the wall.

#### Convection of Wake Vorticity

Each vortex in the flow is convected at the local fluid velocity  $\bar{v}_p$ . The distance that a particular vortex moves in a given time step is obtained using a second-order integration

formula. A simple Euler equation is used for the first time step.

At each time step a new set of vortices is generated along the surface of the body. The initial velocity of these vortices is a function of the strength of the vorticity sheet on the surface, the tangential and normal wall velocities, and the transpiration velocity through the surface.

The vortex rings that represent the vorticity in the flow induce velocities on each other as well as on themselves. In the present formulation, the body moves in an otherwise still fluid. Therefore, the vector velocity  $\bar{v}_P$  at any point  $P$  can be expressed by

$$\bar{v}_P = \sum_{i=1}^{N_v} \bar{v}_{Pi} \quad (10)$$

where,  $\bar{v}_{Pi}$  is the induced velocity vector at point  $P$  due to a vortex at point  $i$ , and  $N_v$  is the total number of vortices in the flowfield.

Since the simulations for bluff bodies require that the wake structure evolve as a function of time (even for "steady flow" calculations), large numbers of vortices ( $100 < N_v < 10,000$ ) are produced. Also, since the wake must be convected as part of the evolution process, the velocity perturbations from all vortices on all other vortices must be calculated at each time step. This requires an amount of work which is proportional to  $N_v^2$  for each time step using direct methods. A fast multipole method which is capable of more efficient calculation of the axisymmetric flowfield produced by a large system of ring vortices has been developed by Strickland and Amos.<sup>11</sup> This method takes advantage of source point and field point series expansions which enables one to make calculations for interactions between groups of vortices which are in well separated spatial domains, rather than having to consider interactions between every pair of vortices. Nondimensional errors for the stream function using this method are on the order of single precision machine accuracy. For 10,000 vortices in the flow, the fast solver obtains solutions in about 1–3% of the time required for the direct solution technique.

#### Surface Pressure Distributions

Once the velocity field has been obtained, the pressure at desired locations in the flow can theoretically be obtained from the Euler equation for an inertially fixed reference frame:

$$\frac{\partial \bar{u}}{\partial t} + (\bar{u} \cdot \nabla) \bar{u} = -\frac{1}{\rho} \nabla p \quad (11)$$

To calculate the surface pressure coefficient for the jump in pressure across the surface of the moving body, Eq. (11) can be written in terms of the coordinate  $s$  and the tangential edge velocities  $U_s^+$  and  $U_s^-$  as shown in Fig. 2

$$\Delta C_p = -\frac{2}{U_0^2} \frac{d\Gamma_s}{dt} \quad (12)$$

where  $U_0$  is an arbitrary reference velocity and

$$\Gamma_s = \int_0^s (U_s^+ - U_s^-) ds \quad (13)$$

The term  $d\Gamma_s/dt$  in Eq. (12) represents the time rate at which circulation is generated and released from the surface between  $s = 0$  and  $s = s$ . It should be noted that  $U_s^+$  and  $U_s^-$  may be evaluated relative to the body surface for use in Eq. (13) since the integrand is the difference in magnitude between two parallel velocity vectors.

#### Example Calculations

A summary of the initial calculation results using the VPARA code are given in this article. Readers who are interested in more details are referred to Ref. 6.

#### General

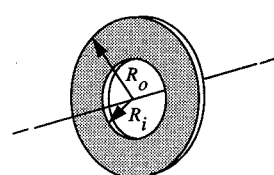
A computer code which embodies the concepts of the previous sections was written and exercised to provide a set of preliminary results. This code is presently designated by the acronym VPARA (Vortex method for PARachutes in Axisymmetric flow). The VPARA code requires an input file which specifies the initial shell geometry. A code was developed as a preprocessor to generate a family of geometries which can be described by axisymmetric segments of an ellipsoid. Thus, slotted and vented disks and hemispheres are a subset of the geometries which can be generated. A motion generator within VPARA specifies the subsequent positions of panel edges at each time step. Presently, the motion subroutine only generates axial rigid-body motions. A series of output files are generated by VPARA at selected time steps which give a "snapshot" description of the surface pressure distribution and the wake geometry, in addition to an up-to-date time history of integrated force coefficients. A code which utilizes the TECPLOT plotting package by Amtec Engineering was developed to postprocess the data.

The present set of calculations consists of 20 simulations of flow over disks with holes and vented hemispherical shells. These geometries were chosen since there is some limited experimental data available for both steady and unsteady flow. The major purpose of these calculations was to develop preliminary insight concerning the predictive capability of VPARA. For instance, the applicability of VPARA to predict bluff-body "axisymmetric" flows which potentially may have non-axisymmetric components of velocity produced by asymmetric instabilities was of interest. The insight developed was incomplete since good quantitative experimental data are very limited, even for these common geometries. Most of the calculations were run on a SUN SPARCstation 1 which provided execution times of about 60 s per time step per 1000 vortices in the flow. A few calculations were run on a SPARC 2 which executed in about 18 s per time step per 1000 vortices in the flow.

#### Disks with Holes

Calculations were made using the VPARA code for disks with various ratios of  $R_i/R_0$ , where  $R_i$  and  $R_0$  are defined in Fig. 3. The disks were discretized into  $N_{PAN}$  panels or annular rings which varied as indicated in the table of Fig. 3. Simulations were made using 200 equal time steps. Values for the nondimensional time step  $U_\infty \Delta t / R_0$  as a function of  $R_i/R_0$  are also given in the table of Fig. 3. The disks were accelerated from rest to a uniform velocity  $U_\infty$  during the first time step in order to simulate an impulsive start.

Typical output from the VPARA code is shown in Fig. 4 for a disk with  $R_i/R_0 = 0.70$ . The body has moved a distance  $x$  along the axis of symmetry of 20 disk radii  $R_0$  to the left. As can be seen from Fig. 4a, alternate shedding is occurring from the annular ring which is similar to the shedding from a two-dimensional flat plate. The instantaneous pressure coefficient  $\Delta C_p$  is shown in Fig. 4b as a function of the distance



$R_i/R_0$	$U_\infty \Delta t / R_0$	$N_{PAN}$
0.00	0.10	20
0.10	0.10	18
0.20	0.10	16
0.40	0.10	12
0.50	0.10	10
0.60	0.10	10
0.70	0.10	10
0.80	0.10	10
0.90	0.05	10

Fig. 3 Disk geometry and simulation parameters.

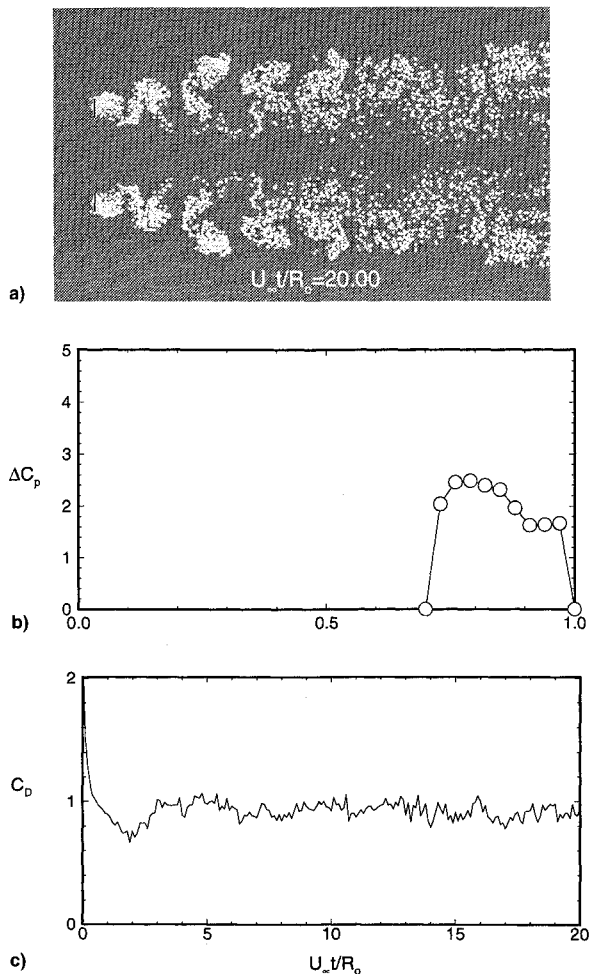


Fig. 4 Typical VPARA output for a vented disk: a) wake geometry, b) pressure distribution, and c) drag coefficient.

s from the axis of symmetry along the surface to some point on the surface. The surface pressure distribution changes constantly due to the unsteady wake. The drag coefficient  $C_D$  is shown in Fig. 4c as a function of the nondimensional time  $U_t/R_0$ . This drag coefficient is based upon the area  $\pi R_0^2$  and the velocity  $U_t$ . Complete drag time histories for each of the cases indicated in Fig. 3 are given in Ref. 6.

In order to estimate the "steady-state" drag obtained from the numerical simulations, the drag data were averaged over the last 120 time steps. Averaging over this range tends to be most adequate for cases with larger values of  $R_i/R_0$ , while being less adequate for cases with lower values. Experimental drag data for disks with holes have been obtained by Hoerner,<sup>12</sup> as well as by Bearman and Takamoto.<sup>13</sup> Hoerner's and Bearman's experiments were run at Reynolds numbers of  $1.0 \times 10^5$  and  $1.4 \times 10^5$ , respectively. These drag data along with the results from the numerical simulation code VPARA are shown in Fig. 5.

Both Hoerner and Bearman note that a fundamental shift in the flow pattern occurs as one increases the radius ratio  $R_i/R_0$  above a certain value. They note that the drag coefficient  $C'_D$  based on the actual disk area as given by Eq. (14) rapidly approaches the drag of a two-dimensional flat plate ( $C'_D \approx 2.0$ ) above a certain value of  $R_i/R_0$ :

$$C_D = C'_D[1 - (R_i/R_0)^2] \quad (14)$$

In the present VPARA simulation, the somewhat abrupt increase in drag coefficient from  $C'_D \approx 1.2$  to  $C'_D \approx 2.0$  with increasing  $R_i/R_0$  was observed to occur simultaneously with the onset of alternate shedding between the inner and outer edges of the rings. The position of this transition region varies between the two sets of data and the numerical simulation.

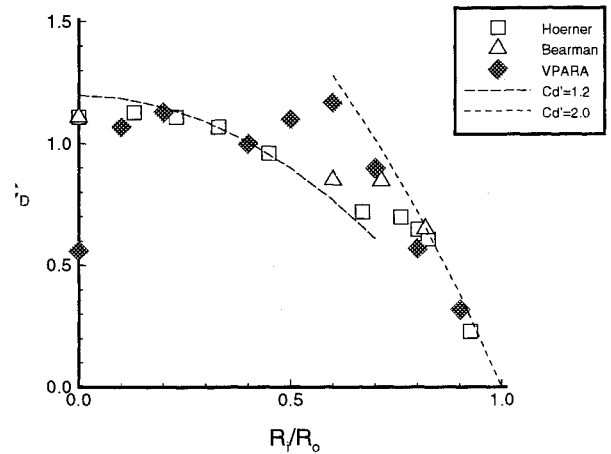


Fig. 5 Disk drag data and simulation.

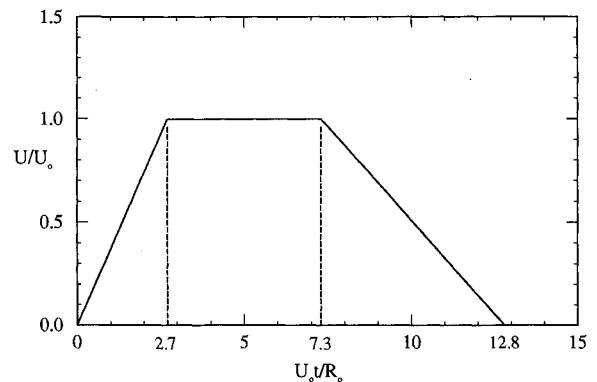


Fig. 6 Velocity time history for Higuchi's flow.

Since the two sets of data were obtained at almost the same Reynolds number, the transition is either very sensitive to Reynolds number or it is sensitive to subtle differences in experimental technique or disk geometry. The VPARA code does not simulate the viscous diffusion process and therefore has no Reynolds number associated with it. Transition for the VPARA code probably depends somewhat on numerical parameters used in the simulation. As a case in point, the reason the time step was reduced for the  $R_i/R_0 = 0.9$  simulation was due to the fact that the larger time step suppressed alternate shedding, which in turn reduced the drag coefficient. In this case, the convection distances apparently became too large with respect to the ring width of  $0.1R_0$ . In any event, prediction of the exact transition region between the two flow patterns appears to be a sensitive issue.

From Fig. 5 it can be noted that the VPARA simulation does not correctly predict the steady-state drag coefficient for a disk without a hole ( $R_i/R_0 = 0.0$ ). Higuchi<sup>14</sup> points out that the wake behind a solid disk eventually becomes asymmetric due to a rotating instability. This rotating instability tends to remove the buildup of vortices from the downstream disk surface, which in turn results in a higher drag coefficient. It can be conjectured that while disks with holes tend not to have a rotating wake instability, the vorticity behind the disk is removed by the axial jet from the hole. It is probable that the VPARA simulation is valid for a solid disk for simulation times prior to the onset of asymmetry.

#### Higuchi's Disk Flow

Higuchi<sup>14</sup> conducted flow visualization experiments on a 4-in.-diam solid disk which was moved in a small towing tank according to the idealized velocity time history shown in Fig. 6. In this experiment, Higuchi injected a mixture of fluorescent dye and neutrally buoyant particles radially through a slot at the edge of the disk. The flow was illuminated from downstream with a thin laser light sheet. In addition, the flow

was illuminated by a pair of black-light fluorescent lamps placed alongside of the tow tank. In the VPARG simulation, discrete ring vortices are shed at many points along the disk surface (18 rings from the front surface plus 18 rings from the rear surface). It should be clear that a direct correlation between the flow visualization pictures of Higuchi and a plot of vortex positions from VPARG cannot be obtained. However, since the major portion of the vortices remain close to the disk surface, except where they separate from the disk edges, one would expect the general shape of the wake formed by the VPARG simulation to resemble that from the flow visualization.

A typical wake shape comparison between the VPARG simulation and the experiment of Higuchi is shown in Fig. 7 for a nondimensional time  $U_0 t/R_0 = 8$ . As can be seen from this figure, the shape of the simulated and experimental wake are roughly the same. Since the vortices are discrete in the VPARG simulation, the streak lines in the experimental flow are not simulated. Thus, the simulated wake does not give one a sense of the center of rotation of the vortex as does the actual flow visualization photograph. Portions of the ring vortices which are out of the laser light plane appear to be illuminated by either reflected laser light from the rear of the disk or perhaps from the black-light fluorescent lamps.

The time history of the drag coefficient calculated using VPARG is shown in Fig. 8 for the Higuchi disk flow. The abrupt rise in the drag coefficient during the first time step is a result of the sudden acceleration of the disk. In fact, the apparent mass  $m_a$  of the disk can be calculated on the basis of this jump in the drag coefficient and the nondimensional acceleration rate to yield a value of  $m_a = 2.72\rho R_0^3$ . The exact value for a disk is given by  $m_a = 2.67\rho R_0^3$ . The abrupt drop in drag coefficient at  $U_0 t/R_0 = 2.7$  is due to the acceleration rate suddenly going to zero. Specification of smoothly varying acceleration rates would eliminate such discontinuities. For nondimensional times greater than 8, the drag coefficient is negative due to the overrunning wake imparting momentum to the disk. Calculated pressure distributions are given in Ref. 6.

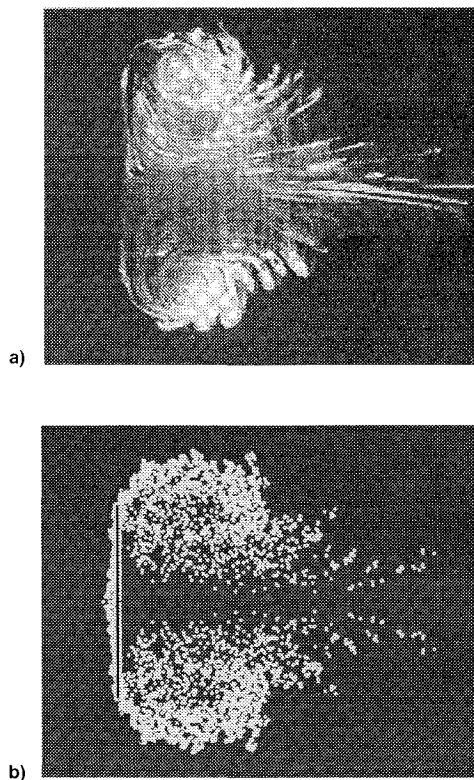


Fig. 7 Wake structure comparison: a) experimental wake and b) VPARG simulation.

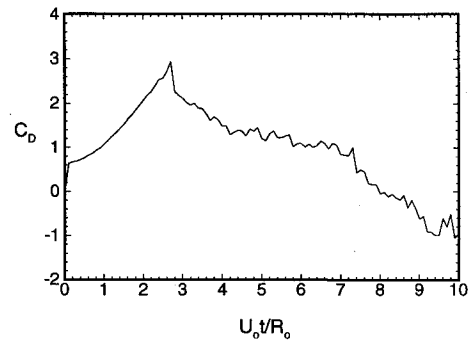


Fig. 8 Calculated drag history for Higuchi disk flow.

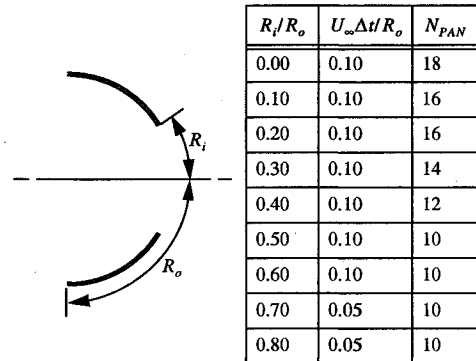


Fig. 9 Hemisphere geometry and simulation parameters.

Calculations were made using the VPARG code for hemispheres with vents for various ratios of  $R_i/R_0$ . The specification of the radii  $R_i$  and  $R_0$  as shown in Fig. 9 is consistent with parachute nomenclature where distances are measured along "the radial." The hemispheres were discretized into  $N_{PAN}$  panels or rings which varied as indicated in the table of Fig. 9. Simulations were made using 200 equal time steps. Values for the nondimensional time step  $U_\infty \Delta t/R_0$  as a function of  $R_i/R_0$  are also given in the table of Fig. 9. The hemispheres were accelerated from rest to a uniform velocity  $U_\infty$  during the first time step.

Typical output from the VPARG code is shown in Fig. 10 for a vented hemispherical shell with  $R_i/R_0 = 0.40$ . The body has moved a distance  $x$  along the axis of symmetry of 20 radii  $R_0$  to the left. As can be seen from Fig. 10a, periodic structures are shed from the vented hemispherical shell. The instantaneous pressure coefficient  $\Delta C_p$  is shown in Fig. 10b as a function of the distance  $s$  from the axis of symmetry along the surface to some point on the surface. The surface pressure distribution changes constantly due to the unsteady wake. The drag coefficient  $C_D$  is shown in Fig. 10c as a function of the nondimensional time  $U_\infty t/R_0$ . This drag coefficient is based upon the area  $\pi R_0^2$  and the velocity  $U_\infty$ . As can be seen from this figure, there is a pronounced periodicity in the drag coefficient time history. The nondimensional fluctuation period  $U_\infty \tau/R_0$  is equal to about 2.0. Complete drag time histories for each of the cases indicated in Fig. 9 are given in Ref. 6. In order to estimate the steady-state drag obtained from the numerical simulations, the drag data were averaged over the last 120 time steps. Averaging over this range would appear to yield representative results. The resulting steady-state drag coefficient calculated using VPARG data is shown plotted in Fig. 11 as a function of  $R_i/R_0$ . According to White,<sup>15</sup> the drag coefficient for a hemispherical shell based on the projected frontal area is approximately 1.4. Therefore, the drag coefficient based on the area  $\pi R_0^2$  is equal to 0.567. For a hemispherical shell with a small vent, one might assume that the pressure distribution along the surface is essentially that of the shell without a vent, except very near the vent itself. If one further assumes that the pressure coefficient is constant

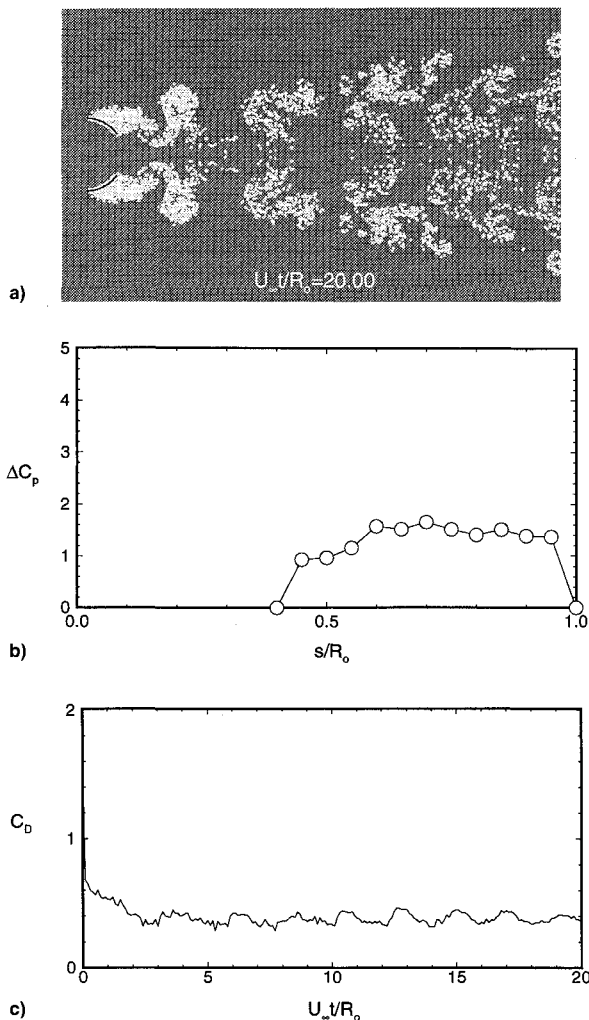


Fig. 10 Typical VPARA output for a vented hemispherical shell: a) wake geometry, b) pressure distribution, and c) drag coefficient.

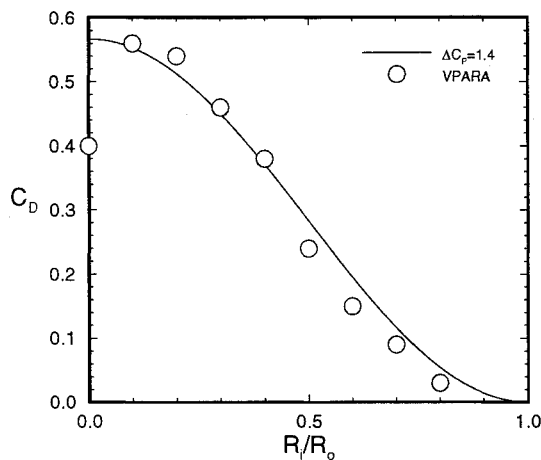


Fig. 11 Drag coefficients for vented hemispherical shells.

along the surface, then an estimate of the drag coefficient for a vented hemispherical shell can be written as

$$C_D = \Delta C_p \left[ \frac{2}{\pi} \cos \left( \frac{\pi R_i}{2 R_0} \right) \right]^2 \quad (15)$$

Equation (15) is plotted in Fig. 11 with  $\Delta C_p$  equal to 1.4, and appears to correlate the VPARA results remarkably well except for shells with very large vent ratios. The presence of the anomalous VPARA prediction at  $R_i/R_0 = 0$  as compared to reasonable results at other vent ratios for the hemispherical

shell can perhaps be explained using the same set of observations as for the circular disk. Those observations included the fact that while the wake is initially axisymmetric, it eventually becomes asymmetric, which tends to remove the buildup of vorticity from the downstream surfaces resulting in a higher drag coefficient. The presence of the vent tends to not only preclude the buildup of vorticity from the downstream surfaces, but it may also stabilize the flow and either prevent asymmetry or at least move the asymmetry far enough downstream such that it does not affect the local flow.

#### Oler's Hemispherical Shell Flow

Recent measurements were made by Oler and Osburn<sup>16</sup> on a 2-ft-diam hemispherical shell which was towed in an 80-ft-long tow tank with a 10- by 15-ft cross section. The velocity time history used for this experiment is shown in Fig. 12. The value of  $U_0$  used in the experiment was 3 ft/s while  $R_0 = \pi/2$  ft. The maximum Reynold's number based on the diameter of the hemisphere was approximately  $6 \times 10^5$ . It should be noted that the shell was being towed at some small nonzero velocity at  $t = 0$ , which resulted in a small deviation between the experimental velocity time history and that used in the VPARA simulation.

The drag time history for this flow is shown in Fig. 13. The drag coefficient  $C_D$  is based on the velocity  $U_0$  and the area  $\pi R_0^2$ . As can be seen from this figure, the experimental data are much smoother than the simulated data. The experimental data have been numerically filtered which accounts for some of the difference in smoothness. As mentioned previously, the VPARA simulation is sensitive to any abrupt changes in acceleration rate which causes some of the jumps in values for the drag coefficient as the shell begins to accelerate. There appears to be a time delay in the experimental data which also may be explained by the numerical filtering (assuming that a backward averaging scheme was used). In general, however, the agreement between the experimental data and the VPARA simulation is acceptable.

#### Conclusions and Recommendations

Based on comparisons between the limited set of flow simulations and the even more limited set of associated experimental data, it appears that the VPARA code holds reasonable promise for development into an aeroprediction code for

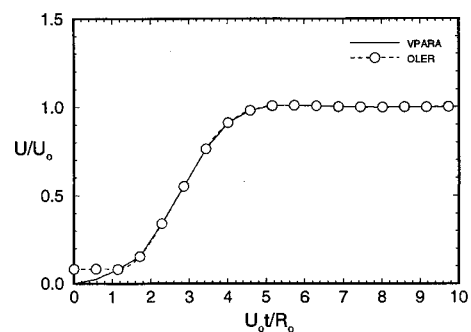


Fig. 12 Velocity time history for Oler's hemispherical shell flow.

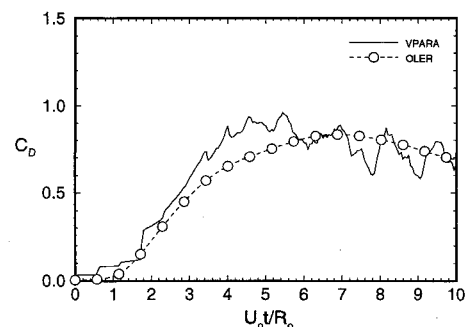


Fig. 13 Drag time history for Oler's hemispherical shell flow.

parachute inflation. A mature version of this code will allow one to carry out a significant percentage of the simulations which will be required in the design of parachute systems, even though this code is restricted to axisymmetric incompressible flow situations. The apparent restriction on the code's ability to calculate correct steady-state pressure and drag coefficients for unvented shells due to the onset of wake asymmetry fortunately does not have a major impact on the parachute inflation problem, since axisymmetric parachutes are always vented and since inflation takes place during the first 10–15 diameters of travel.

The VPARA code will require additional development and benchmarking before it can be used as part of an inflation code. A vortex merge capability and the surface porosity modeling are the most important features which need to be fully implemented. A considerable amount of benchmarking must be done to develop rules which can be used to automatically set time step sizes during simulation. Guidelines for properly sizing panels must also be developed. In order for the VPARA code to be useful in predicting parachute inflation, a dynamics code must be coupled into VPARA through the motion generator subroutine. It is envisioned that the dynamics code will calculate the inertial loads of the payload, the suspension lines, and the canopy fabric, and balance these through appropriate equations of motion to the aerodynamic loads on the canopy.

### Acknowledgment

This work performed at Sandia National Laboratories was supported by the U.S. Department of Energy under Contract DE-AC04-76DP00789.

### References

<sup>1</sup>Clements, R. R., and Maull, D. J., "The Representation of Sheets of Vorticity by Discrete Vortices," *Progress in Aerospace Sciences*,

Vol. 16, No. 2, 1975, p. 129.

<sup>2</sup>Sarpkaya, T., "Computational Methods with Vortices," *Journal of Fluid Engineering*, Vol. 111, No. 1, 1989, pp. 5–52.

<sup>3</sup>Saffman, P. G., and Baker, G. R., "Vortex Interactions," *Annual Review of Fluid Mechanics*, Vol. 11, 1979, pp. 95–122.

<sup>4</sup>Leonard, A., "Vortex Methods for Flow Simulation," *Journal of Computational Physics*, Vol. 37, No. 3, 1980, pp. 289–335.

<sup>5</sup>Sarpkaya, T., "Unsteady Flow About Porous Cambered Shells," *Journal of Aircraft*, Vol. 28, No. 8, 1991, pp. 502–508.

<sup>6</sup>Strickland, J. H., "Axisymmetric Bluff-Body Flow: A Vortex Solver for Thin Shells," Sandia National Lab. Rept. SAND91-2760, Albuquerque, NM, May 1992.

<sup>7</sup>Currie, I. G., *Fundamental Mechanics of Fluids*, McGraw-Hill, New York, 1974, p. 46.

<sup>8</sup>Lamb, H., *Hydrodynamics*, 6th ed., Dover, New York, 1945, pp. 236–241.

<sup>9</sup>Koo, J. K., and James, D. F., "Fluid Flow Around and Through a Screen," *Journal of Fluid Mechanics*, Vol. 60, Pt. 3, 1973, pp. 513–538.

<sup>10</sup>Taylor, G. I., and Batchelor, G. K., "The Effect of Wire Gauze on Small Disturbances in a Uniform Stream," *Quarterly Journal of Mechanics and Applied Mathematics*, Vol. 2, Pt. 1, 1949, pp. 1–29.

<sup>11</sup>Strickland, J. H., and Amos, D. E., "Fast Solver for Systems of Axisymmetric Ring Vortices," *AIAA Journal*, Vol. 30, No. 3, 1992, pp. 737–746.

<sup>12</sup>Hoerner, S. F., *Fluid-Dynamic Drag*, published by the author, 1965, pp. 3–16.

<sup>13</sup>Bearman, P. W., and Takamoto, W., "Vortex Shedding Behind Rings and Disks," *Fluid Dynamics Research*, Vol. 3, Nos. 1–4, 1988, pp. 214–218.

<sup>14</sup>Higuchi, H., "Wake Behind a Circular Disk in Unsteady and Steady Incoming Streams," AIAA Paper 91-0852, April 1991.

<sup>15</sup>White, F. M., *Fluid Mechanics*, McGraw-Hill, New York, 1979, p. 436.

<sup>16</sup>Oler, J. W., and Osburn, A., "Force Measurements on Bodies Undergoing Unsteady Motions in a Tow Tank," Sandia National Lab. Rept. SAND89-7150, Albuquerque, NM, July 1993; also Osburn, A., "Force Measurements for Tow Tank Measurements," M.S. Thesis, Texas Tech Univ., Lubbock, TX, May 1993.